Electronic Supplementary Material (ESI) for Journal of Materials Chemistry C.

Supplementary material:

Thermal conductivity of sliding bilayer *h*-BN and its manipulation with strain and layer confinement

Yi-Ming Zhao[a], *Chun Zhang*[b,c], *Sunmi Shin*[a]*, *Lei Shen*[a]*

[a]Department of Mechanical Engineering, National University of Singapore, 9 Engineering Drive 1, Singapore 117575

[b]Department of Physics, Faculty of Science, National University of Singapore, 2 Science Drive 3, Blk S12, Level 2, Singapore 117542

[c]Department of Chemistry, National University of Singapore, Block S8 Level 3, 3 Science Drive 3, Singapore 117543

*mpeshin@nus.edu.sg; *shenlei@nus.edu.sg

1. CALCULATIONAL DETAILS

For the monolayer, bilayer and tri-layer *h*-BN, we set the vacuum slab as 20 Å to avoid the interaction between different unit cells in the out-of-plane direction. Both the lattice parameters and atomic positions were first relaxed until the interatomic forces are smaller than 10^{-4} eV/ Å in the structural relaxation. Then, the atomic positions were further relaxed with fixed lattice parameter until the forces are smaller than 10^{-6} eV/ Å to obtain an accurately optimized structure with no imaginary phonon frequency.

To calculate the electronic structures, we implemented the calculation with a 20×20×1 (16×16×4 for bulk structure) K-point mesh, 600 eV cut-off energy and 10^{-8} eV energy convergence threshold. For the calculation of phonon band structures with the finite displacement method, the supercell size was set as 5×5×1 (5×5×2 for bulk structure) to generate the structures with displaced atoms and the K-point mesh was 5×5×1 (5×5×3 for bulk structure). In the calculation of the third order force constants, the supercell size was 5×5×1 (4×4×2 for bulk structure) and the number of nearest neighbors considered was 19 based on the convergence test, while the self-consistent calculation for each displaced structure was implemented in Gamma point for K-point sampling. Finally, we implemented the thermal conductivity calculation with Gaussian smearing of 0.5 and a dense grid sampling of 100×100×1 (bilayer), 70×70×1 (tri-layer) and 40×40×10 (bulk). The electron relaxation time is calculated by interpolating the DFT based band structure (27×27×1) with a very

dense K-point mesh of 180×180×1 with EPW code to obtain more accurate Seebeck coefficient and electrical conductivity results.

2. BILAYER *h*-BN

There are five different configurations of bilayer *h*-BN as listed in **Figure S1**. Note that AB and BA configurations are identical structures but in different spatial views. The AB' and AC' correspond to configurations by sliding the antiparallel AA' in opposite directions. The AB and BA are configurations by sliding the parallel AA configuration left and right. In the AA' configuration, the N atoms are on the top of B atoms (N-B) similar to AB. Half of the N or B atoms in the AB configuration are at the center of hexagon. In the AC' configuration, the B atoms are on the top of B atoms and the N atoms sit on the center of the hexagon. In the AA configuration, the two atomic layers are parallel to each other and the N (B) atoms are on the top of N (B) atoms (N-N, B-B). In the AB' configuration, the N atoms are on the top of N atoms (N-N) and B atoms are in the center of the hexagon.

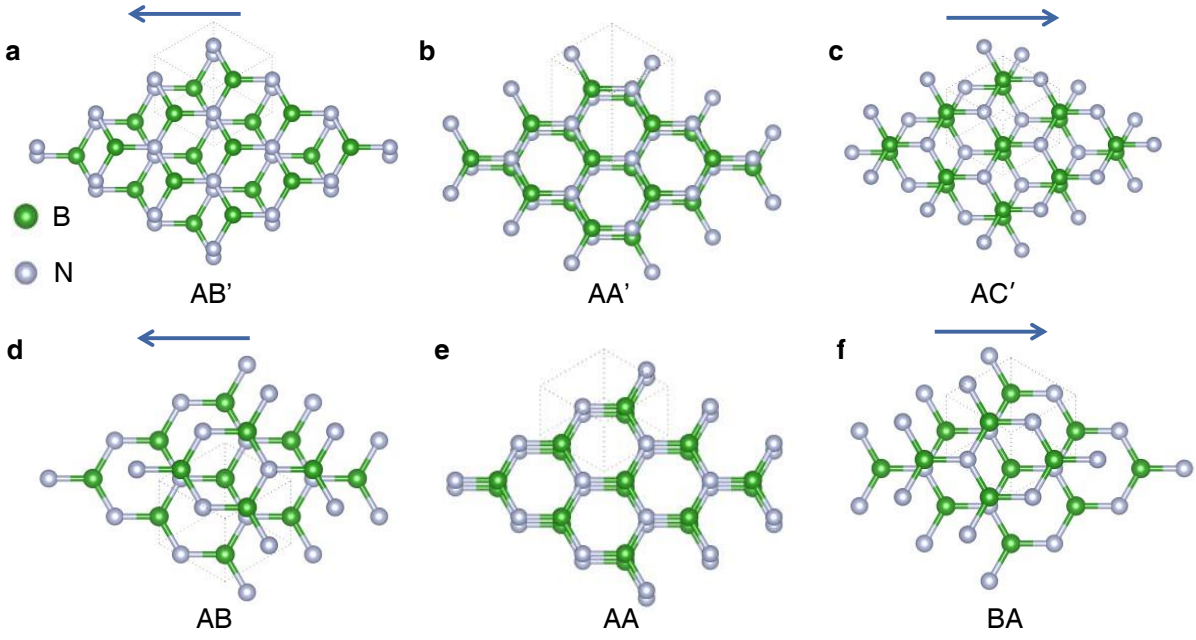

Figure S1 | Supercell structures of bilayer *h*-BN with different stacking patterns. The blue arrows indicate the sliding directions.

There are tiny imaginary frequencies in the configuration of AB' and AA configuration, as shown in **Figure S2**. The N-N stacking patterns in the two structures are unstable due to the stronger electronegativity of N elements. The other three bilayer structures are stable with no imaginary frequencies.

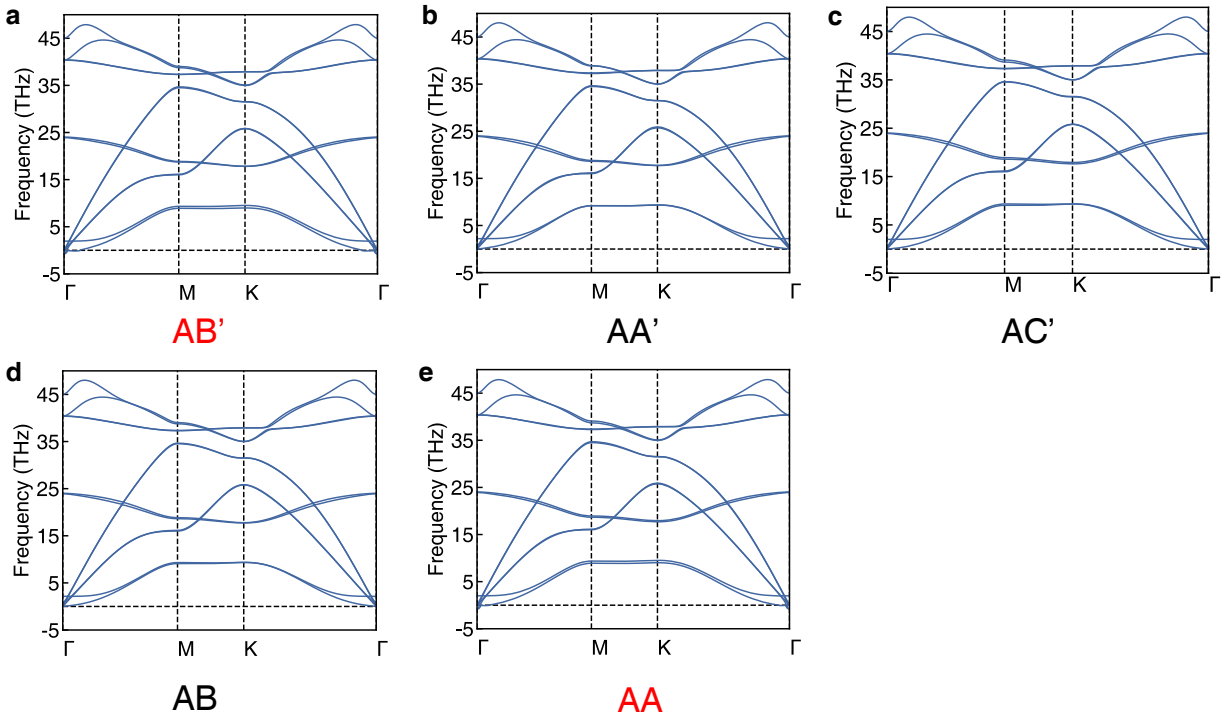

Figure S2 | Phonon band structures of bilayer h-BN with different stacking patterns, **a** AB', **b** AA', **c** AC', **d** AB and **e** AA. Note that the phonon band structure of BA is not shown here as it is identical to AB. The AB' and AA configurations have the imaginary frequency, indicating dynamically unstable.

The initial phonon relaxation time is positive but some part of the final converged phonon relaxation time is negative near the frequency of 15 THz. Hence, the negative phonon relaxation time should be a numerical artifact during the iterative process. The negative phonon relaxation time leads to a negative κ value.

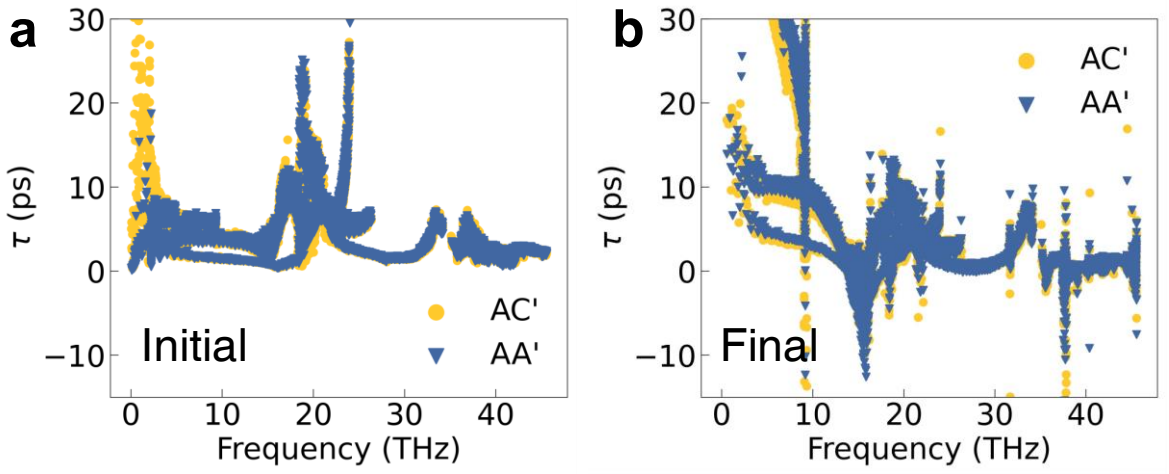

Figure S3 | a and **b** are the phonon relaxation time before and after the iteration process.

The frequency differences of TO and LO modes near the Γ point also contribute to the different κ value of AA' and AC'. The total phonon scattering rate of AC' in **Figure STOLO** is obviously larger than that of AA' consistent with the lower κ of AC'.

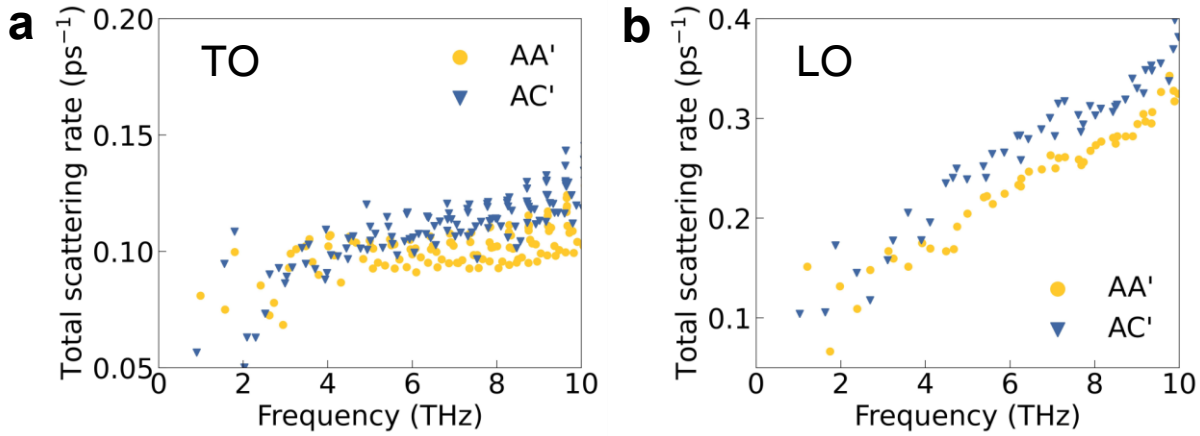

Figure S4 | a and **b** are the total scattering rate of TO and LO modes.

To further check the atomic vibration properties of different stacking configurations, we run the ab initio molecular dynamics (AIMD) simulations at the temperature of 300 K using the structures in **Figure S5 a and b**. The surrounding atoms are fixed manually to avoid the automatic sliding in the simulation process as the energy barrier for sliding is only 26 meV per unit cell [1]. The in-plane vibration amplitude of AC' is obviously larger than that of AA' as shown in Figure SAIMD c. As a result, the variation of force for the AC' structure is also larger compared with AA'. The larger vibration amplitude of AC' indicate a larger lattice anharmonicity and lower κ value.

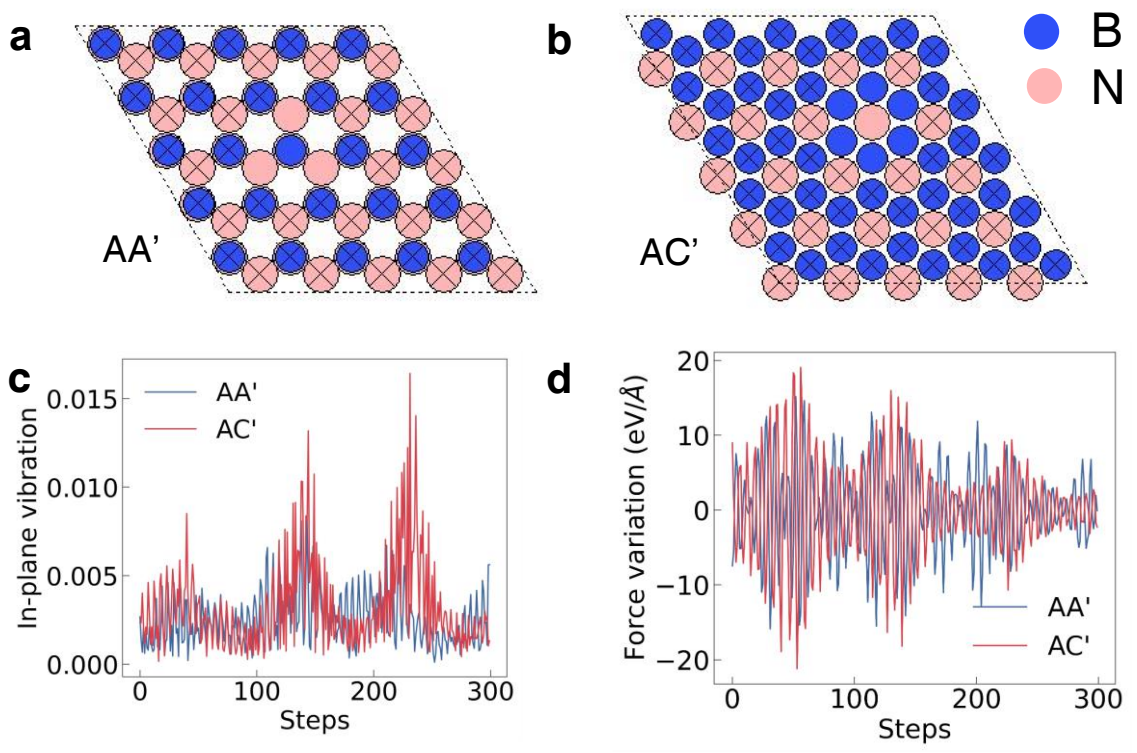

Figure S5 | **a** and **b** are the structures of AA’ and AC’ for ab initio molecular dynamics (AIMD) simulation. The atoms with cross marks are fixed during the simulation steps. **c** the in-plane atomic vibration amplitude. d the force variation during the simulation steps.

We calculate the phonon mean free path (MFP) by multiplying the phonon relaxation time (τ) and the group velocity (v_g), MFP= $\tau \bullet v_g$ as shown in **Figure S6** [2]. The phonon relaxation time is the inverse of the phonon scattering rate as shown in **Figure S6a**. The phonon group velocity reflects the slope of the phonon spectrum as shown in **Figure S6b**. The largest phonon MFPs are about 300 nm with the frequency around 20 THz as shown in **Figure S6c**. From the cumulative κ results, the phonon with MFP smaller than 10^3 nm contribute most to the final κ as shown in **Figure S6d** close to the results of bluk h-BN [3]. The phonon MFP values in **Figure S6c** and **d** are in the same magnitude, which indicates the calculation of phonon MFP in **Figure S6c** is reasonable.

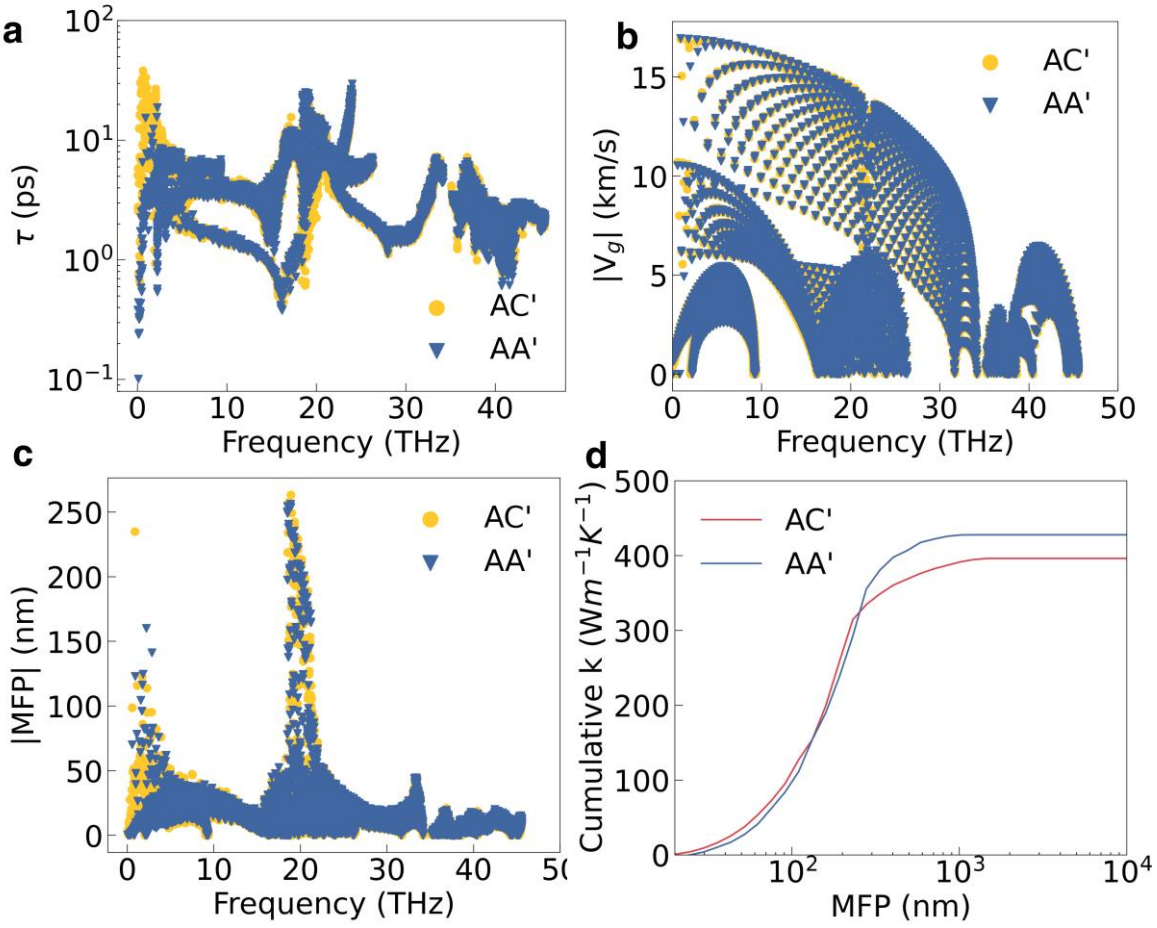

Figure S6 | **a** The phonon relaxation time (τ) of AC' and AA'. **b** The absolute value of phonon group velocity (v_g). **c** The absolute value of phonon mean free path (MFP) as a function of frequency. **d** The cumulative thermal conductivity (κ) with the increasing of phonon MFP.

The electron relaxation time (τ_e) is calculated from the imaginary part of electron self-energy based on the electron-phonon coupling as shown in **Figure S7a** [4].

$$\frac{1}{\tau_{nk}} = \frac{2\pi}{\hbar}\sum_{mv}\int_{BZ}\frac{d\boldsymbol{q}}{\Omega_{BZ}}\left|g_{mn,v}(k,q)\right|^2 \times \{[n_{qv}+f_{mk+q}]\delta(\omega-(\varepsilon_{mk+q}-\varepsilon_f)+\omega_{qv})+ [n_{qv}+1-f_{mk+q}]\delta(\omega-(\varepsilon_{mk+q}-\varepsilon_f)-\omega_{qv})\} \quad \text{(S1)}$$

where m and n are the index of each electron bands, k and q represent the electron and phonon wave vector, v indicates the branch of phonon bands, f and n are the electron and phonon distribution function, ω and ε represent the phonon frequency and the energy of electron bands. The τ_e of AC' is obviously larger than that of AA'. Then, we calculate the thermoelectric properties like Seebeck coefficients (S) and electric conductivity (σ) based on the τ_e by solving the Boltzmann transport equation using BoltzTraP code[5]. The power factor (PF) is the product of S and σ ($PF=S^2\sigma$) as shown in **Figure S7b**. The PF of AC' is larger than AA' under p-type doping due to the larger σ, while smaller under n-type doping due to the smaller S.

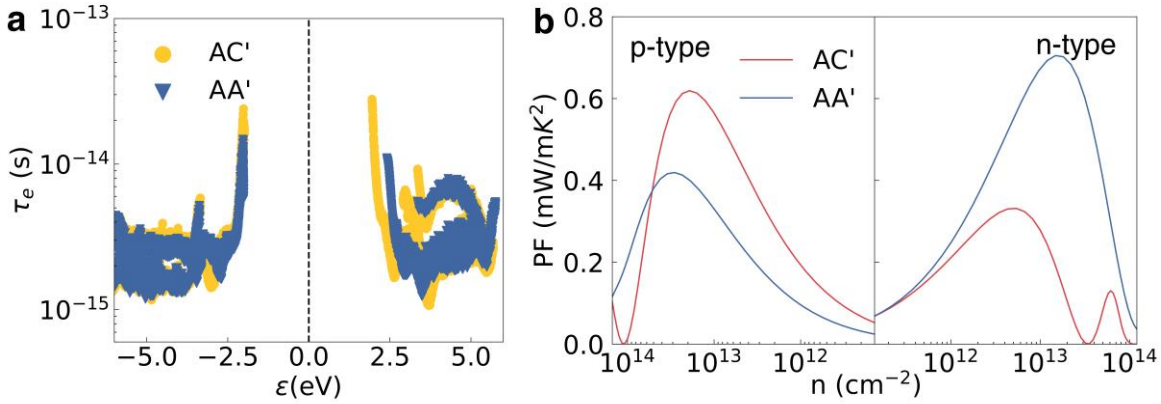

Figure S7 | **a** The electron relaxation time (τ_e) of AA' and AC' with respect to the energy. **b** The power factor of AA' and AC' under different doping concentrations.

The electronic structure of the AB configuration is similar to that of AA' as the stacking patterns in the two configurations are similar, as shown in **Figure S8**. However, only half atoms are on the top site in AB lead to weaker interlayer interaction compared with AA' and more degenerate band levels both in conduction band minimum (CBM) and valence band maximum (VBM).

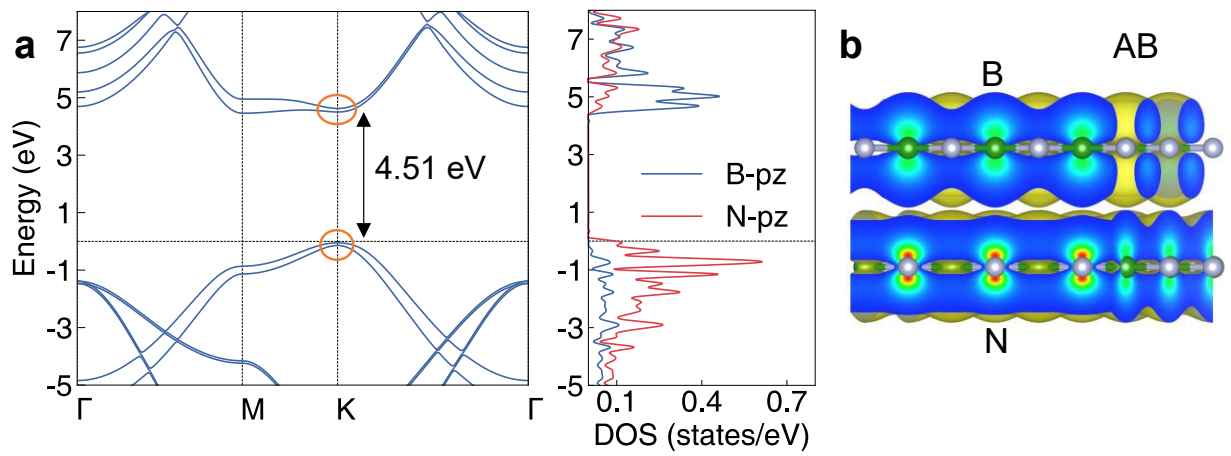

Figure S8 | **a** The electronic band structure and density of states of bilayer h-BN with AB type stacking pattern. **b** the band decomposed charge density corresponds to the CBM and VBM in K point as circled in the band structure.

The weighted phase space directly depends on the phonon dispersion relation from the equation S2 and S3 [6].

$$W_{\lambda}^{+} = \frac{1}{2N}\sum_{\lambda' p''} \frac{2(f_{\lambda'} - f_{\lambda''})}{\omega_{\lambda}\omega_{\lambda'}\omega_{\lambda''}}\delta(\omega_{\lambda} + \omega_{\lambda'} - \omega_{\lambda''}); \quad \text{(S2)}$$

$$W_{\lambda}^{-} = \frac{1}{2N}\sum_{\lambda' p''} \frac{f_{\lambda'} + f_{\lambda''} + 1}{\omega_{\lambda}\omega_{\lambda'}\omega_{\lambda''}}\delta(\omega_{\lambda} + \omega_{\lambda'} - \omega_{\lambda''}), \quad \text{(S3)}$$

where W represents the WP3 and p represents the specific phonon branch. The symbol + or – means the absorption or emission process, respectively. N is the total number of sampling points in the Brillouin zone (BZ). ω_{λ} represents the frequency of phonon modes λ and f_{λ} is the Bose-Einstein distribution. The δ function ensures the phonon scattering follows the energy conservation rule.

While the anharmonic scattering rate (ASR) both depends on the phonon dispersion relation and the interatomic force constants as shown in equation S4 and S5.

$$\Gamma^{+}_{\lambda\lambda'\lambda''} = \frac{\hbar\pi}{8N}\frac{2(f_{\lambda'}-f_{\lambda''})}{\omega_{\lambda}\omega_{\lambda'}\omega_{\lambda''}}\delta(\omega_{\lambda}+\omega_{\lambda'}-\omega_{\lambda''})\left|V^{+}_{\lambda\lambda'\lambda''}\right|^{2}; \quad \text{(S4)}$$

$$\Gamma^{-}_{\lambda\lambda'\lambda''} = \frac{\hbar\pi}{8N}\frac{f_{\lambda'}+f_{\lambda''}+1}{\omega_{\lambda}\omega_{\lambda'}\omega_{\lambda''}}\delta(\omega_{\lambda}-\omega_{\lambda'}-\omega_{\lambda''})\left|V^{-}_{\lambda\lambda'\lambda''}\right|^{2}, \quad \text{(S5)}$$

where Γ represents the three-phonon transition possibilities and the sum of Γ is the ASR. The main difference between WP3 and ASR is the scattering matrix element V depending on the anharmonic interatomic force constants (IFC)[7]:

$$\mathrm{V}^{\pm}_{\lambda\lambda'\lambda''} = \sum_{i\epsilon u.c}\sum_{j,k}\sum_{\alpha\beta\gamma}\Phi^{\alpha\beta\gamma}_{ijk}\frac{e^{\alpha}_{\lambda}(i)e^{\beta}_{p',\pm q'}(j)e^{\gamma}_{p'',-q''}(k)}{\sqrt{M_i M_j M_k}}, \quad \text{(S6)}$$

where the *i, j* and *k* are the atomic indices and α, β and γ are the Cartesian coordinates. $e_{\mathrm{p,\,q}}$ denotes the normalized eigenfunctions of the involved phonons.

The anharmonic scattering rate (ASR) of AC' configuration under the -10% is smaller compared with the strain of -8% and -12% as shown in Figure S9. The local minimum value of ASR lead to a local maximum κ value. The strain does not influence the anharmonic phonon scattering and the κ in a monotonic way.

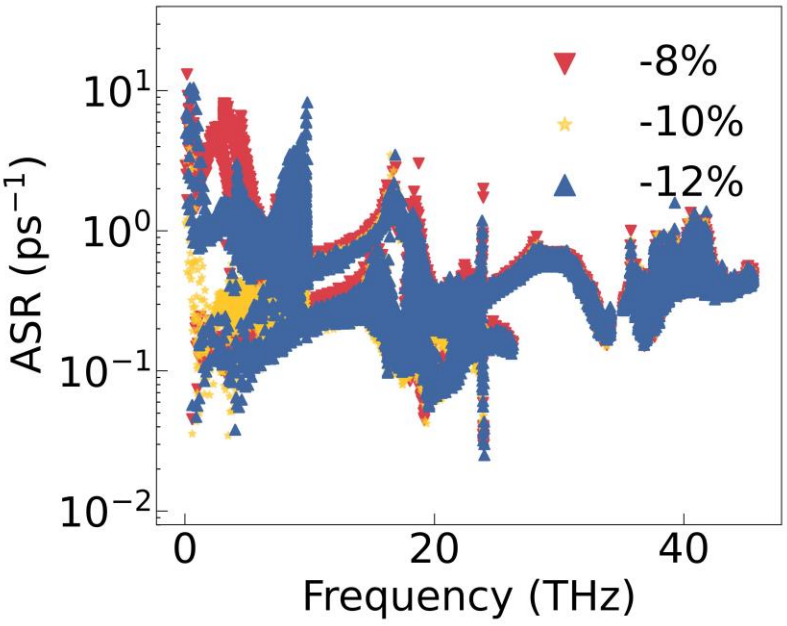

Figure S9 | The anharmonic scattering rate of AC' configuration under the strain of 8%, 10% and 12%.

In a narrow frequency range of 0-4 THz, the magnitude of Grüneisen parameter (γ) gets smaller as the strain increase from 0% to 18% as shown in **Figure S10**. Such a small narrow-range change results in a weak influence on the total thermal conductivity (0-50 THz). The small magnitude of γ under the 18% strain is consistent with the suppressed anharmonic scattering rate and high thermal conductivity under this condition as shown in **Figure 5** in the main text.

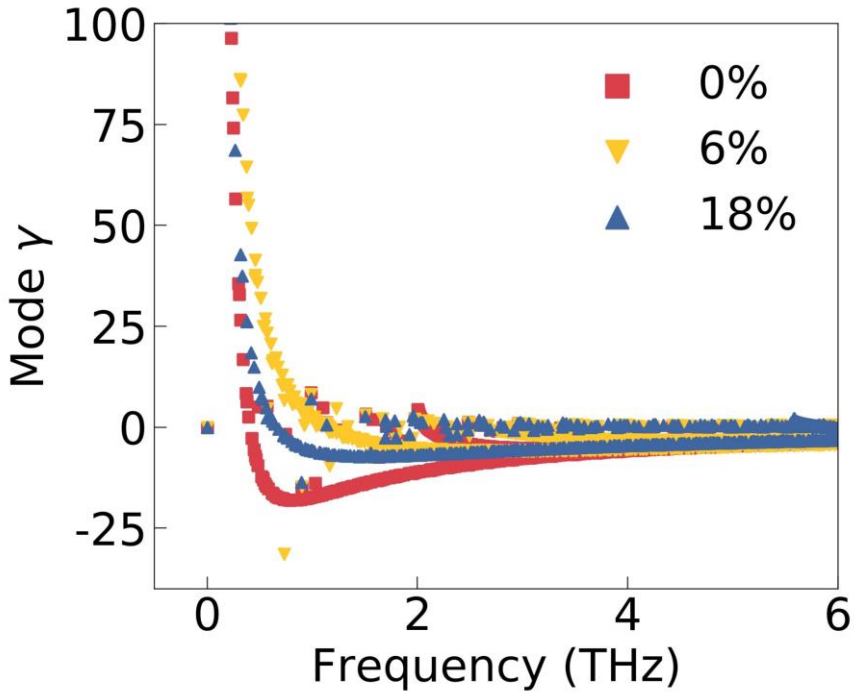

Figure S10 | The Grüneisen parameter (γ) of AC' configuration under different out-of-plane strain from 0% to 18%.

For the configurations of AA' and AB, the frequencies of ZO' modes also increase with the increasing out-of-plane strain as shown in **Figure S11**. But there are obvious imaginary frequencies under the strain of 6% and 12% indicating the structures are unstable under such strains. We only calculate the κ for the configurations with strain below 6%.

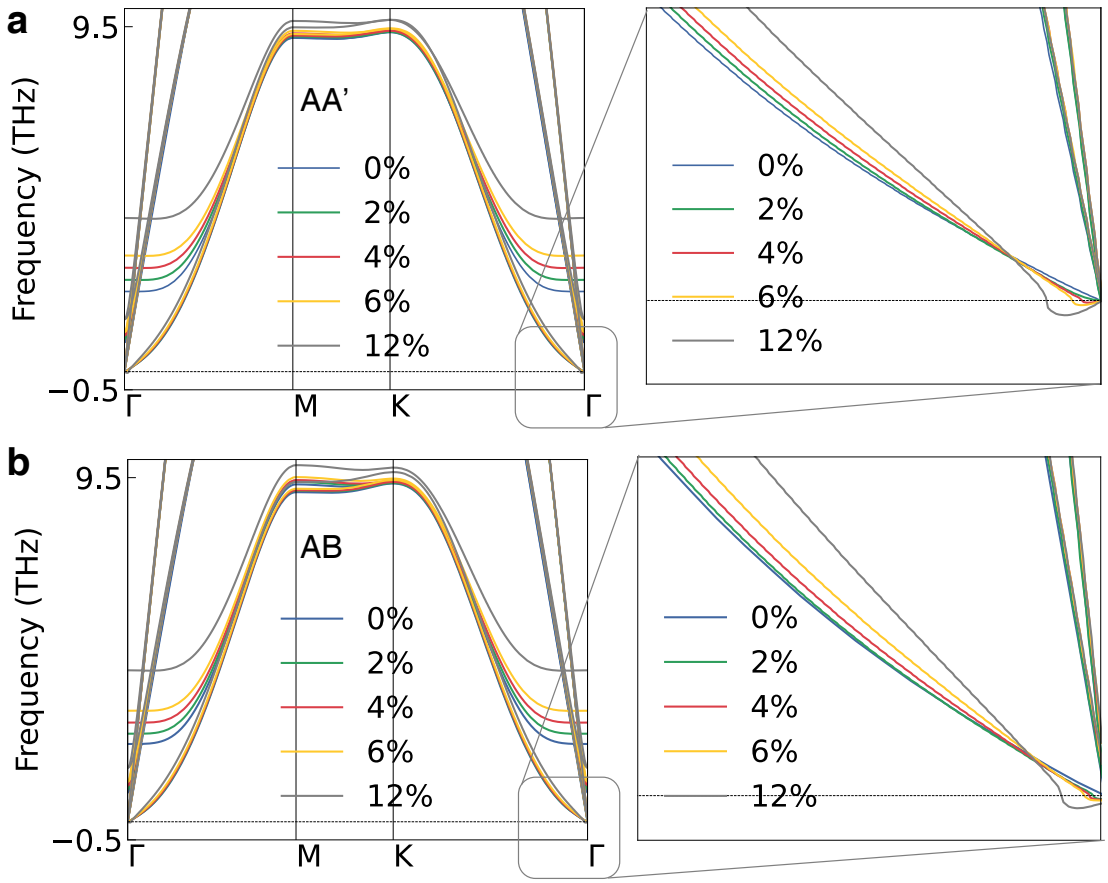

Figure S11 | The phonon band structure of AA' (**a**) and AB (**b**) under out-of-plane strain from 2% to 12%.

The κ of AA' decrease with the increasing strain (smaller than 6%) similar to the case of AC' as shown in **Figure S12a**. The increasing anharmonic scattering rate (ASR) is consistent with the decreasing κ value as shown in **Figure S12b**. The out-of-plane strain enhances the lattice anharmonicity and lead to a decreasing κ for AA' and AC'. The κ of AB configuration only decrease slightly and the ASR of AB do not increase obviously, which is different from AA' and AC' as shown **Figure S12a** and **c**. In AA', all the N (B) atoms in the upper layer are on the top site of the B (N) atoms in the bottom layer, which induce a stronger B-N van der Waals interaction

and a higher ASR under strain. The higher ASR or lower phonon relaxation time of AA' cause a lower κ compared with AB configuration.

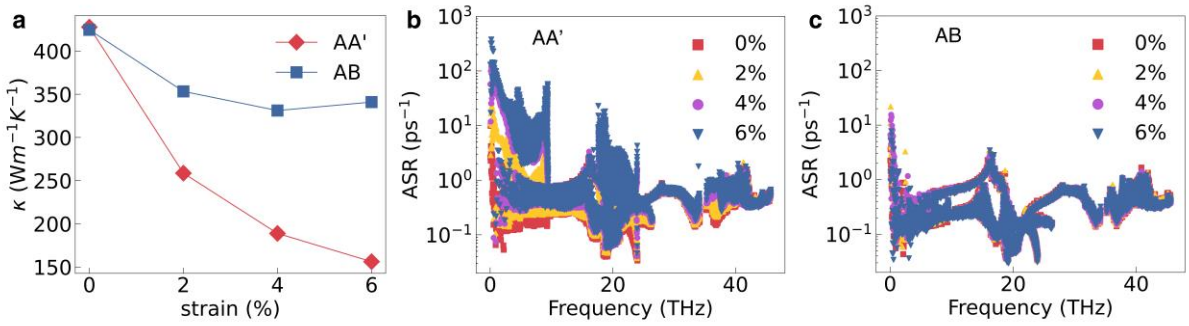

Figure S12 | a The κ of AA' and AB vary with the applied strain. **b** and **c** are the anharmonic scattering rate (ASR) of AA' and AB under different strains.

3. TRI-LAYER h-BN

For tri-layer structures, we consider the same bilayer stacking patterns, i.e., AA', AB, and AC' as the building-block to build tri-layer structures (**Figure S13**). In AA'(A)-type, all the B (N) atoms in the middle layer are sandwiched by the N (B) atoms in adjacent layers (N-B). In AB(A)-type, the B atoms in the middle layer are on the site just sandwiched by the N atoms in adjacent layers (N-B), while the N atoms are in the center of the hexagon. In AC'(A)-type, the B atoms in the middle layer are just sandwiched by the B atoms in adjacent layers (B-B), while the N atoms are in the center on the hexagon.

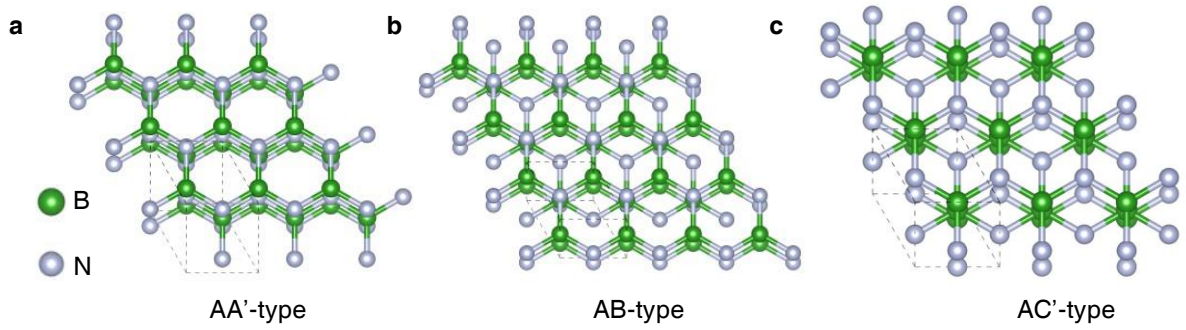

Figure S13 | The supercell structure of tri-layer *h*-BN with the **a** AA'(A), **b** AB(A) and **c** AC'(A)-type configuration.

For the tri-layer and bulk structures, the phonon frequencies of AC' are still lower than that of AA' and AB as shown in **Figure S14**, which are the same as the bilayer case. There are more phonon modes in the phonon band structure of tri-layer due to more atoms in the tri-layer primitive cell.

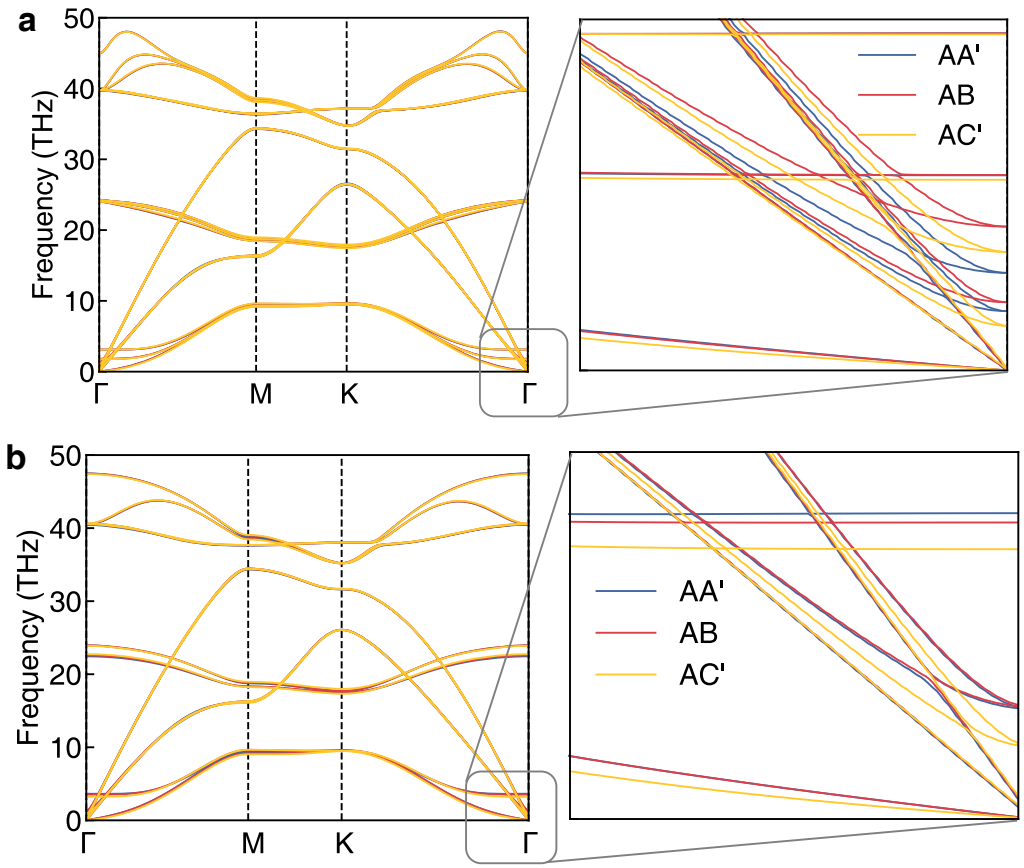

Figure S14 | The phonon band structures of **a** tri-layer structures and **b** bulk structures with three stacking patterns: AA', AB and AC'.

From the bilayer to tri-layer and bulk structure, the anharmonic scattering rate of AC' gets more deviation from that of AA' as shown in **Figures S15a**, **b** and **c.** The deviation of the Grüneisen parameter (γ) of AC' and AA' also becomes larger and larger from bilayer to tri-layer and bulk structures as shown in **Figures S15d**, **e** and **f**. The clear differences mostly lie in the narrow frequency range from 0 THz to 4 THz. The larger difference indicates that the confinement of more layers enhances the difference of the thermal transport behavior between AC' and AA' type configurations.

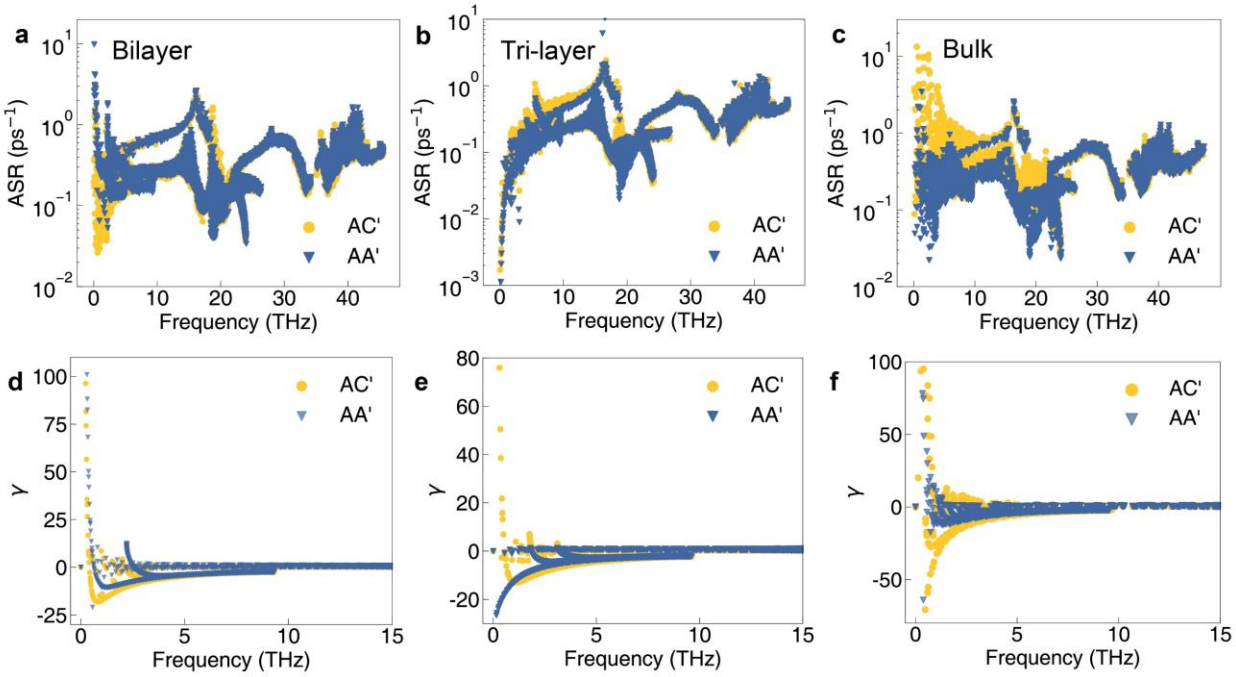

Figure S15 | **a**, **b** and **c** are the anharmonic scattering rate (ASR) of bilayer, tri-layer and bulk structures with AC' and AA' type stacking patterns. **d**, **e** and **f** are the Grüneisen parameter (γ) for the three structures.

For bilayer configurations, the difference between AA' and AB of the weighted phase space, Grüneisen parameter (γ) and converged total scattering rate is almost negligible as shown in **Figures S16a**, **b** and **c**. However, such difference is slightly larger in the bulk structures in **Figures S16d**, **e** and **f.** The weighted phase space and the scattering rate of AA' is larger than that of AB, which is the origin of the lower thermal conductivity of AA'. It is because in the bulk structure with the AA' configuration, all atoms in the upper layer are on the top site of the atoms in the lower layer, while only half atoms overlap between the two layers in the AB configuration. More head-to-head atoms have a high scattering possibility and a large total scattering rate as shown in **Figures S16d** and **f**. Therefore, the thermal conductivity of bulk AA' configuration is lower than that of the AB configuration.

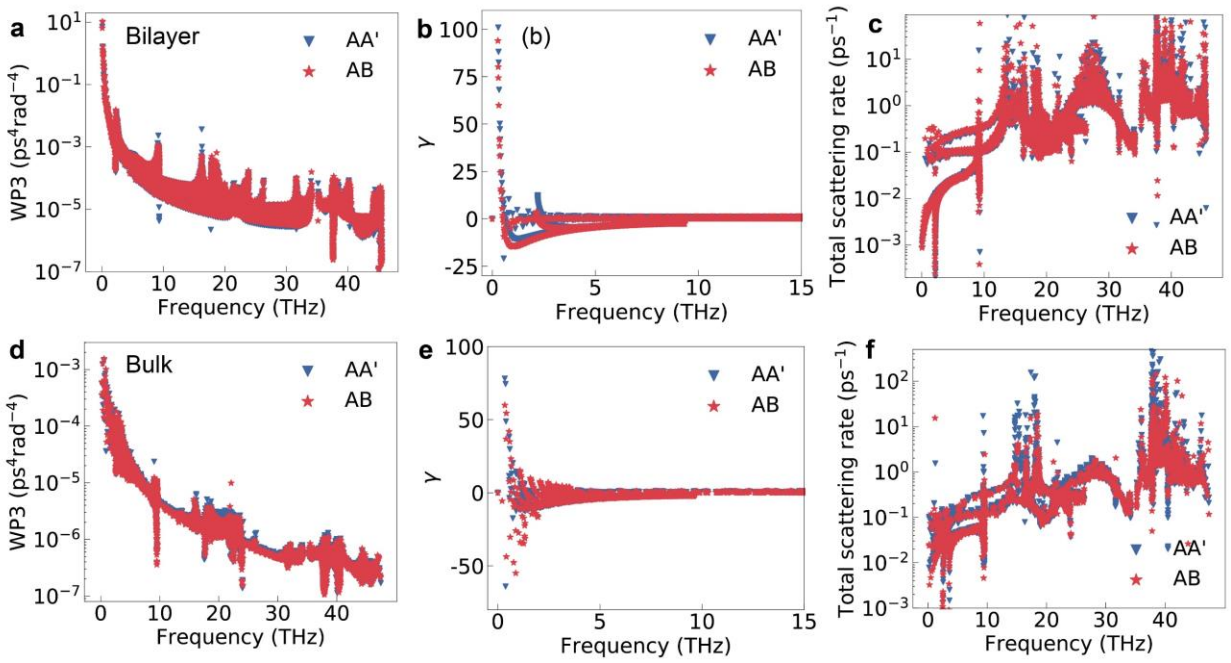

Figure S16 | a, **b** and **c** are the weighted phase space (WP3), Grüneisen parameter (γ) and converged total scattering rate of AA' and AB configuration in bilayer structures. **d**, **e** and **f** are the corresponding quantities for AA' and AB in bulk structures.

REFERENCES

[1] N. Marom, J. Bernstein, J. Garel, A. Tkatchenko, E. Joselevich, L. Kronik, and O. Hod, Stacking and Registry Effects in Layered Materials: The Case of Hexagonal Boron Nitride, Phys. Rev. Lett. **105**, 046801 (2010).
[2] G. Barbalinardo, Z. Chen, H. Dong, Z. Fan, and D. Donadio, Ultrahigh Convergent Thermal Conductivity of Carbon Nanotubes from Comprehensive Atomistic Modeling, Phys. Rev. Lett. **127**, 025902 (2021).
[3] P. Jiang, X. Qian, R. Yang, and L. Lindsay, Anisotropic thermal transport in bulk hexagonal boron nitride, Phys. Rev. Mater. **2**, 064005 (2018).
[4] S. Poncé, E. R. Margine, C. Verdi, and F. Giustino, EPW: Electron–phonon coupling, transport and superconducting properties using maximally localized Wannier functions, Comput. Phys. Commun. **209**, 116 (2016).
[5] G. K. H. Madsen and D. J. Singh, BoltzTraP. A code for calculating band-structure dependent quantities, Comput. Phys. Commun. **175**, 67 (2006).
[6] W. Li and N. Mingo, Ultralow lattice thermal conductivity of the fully filled skutterudite $YbFe_4Sb_{12}$ due to the flat avoided-crossing filler modes, Phys. Rev. B **91**, 144304 (2015).
[7] W. Li, J. Carrete, N. A. Katcho, and N. Mingo, ShengBTE: A solver of the Boltzmann transport equation for phonons, Comput. Phys. Commun. **185**, 1747 (2014).